J. Fluid Mech. (2019), *vol.* 862, *pp.* 753–780.
doi:10.1017/jfm.2018.965

Rough or wiggly? Membrane topology and morphology for fouling control

Bowen Ling[1] **and Ilenia Battiato**[1,†]

[1]Energy Resources Engineering, Stanford University, Stanford, CA 94305, USA

(Received 7 August 2018; revised 26 October 2018; accepted 22 November 2018)

During filtration in reverse osmosis membranes (ROM), the system performance is dramatically affected by membrane fouling which causes a significant decrease in permeate flux as well as an increase in the energy input required to operate the system. In this work, we develop a model, able to dynamically capture foulant evolution, that couples the transient Navier–Stokes and the advection–diffusion equations, with an adsorption–desorption equation for the foulant accumulation. The model is validated against unsteady measurements of permeate flux as well as steady-state spatial fouling patterns. For a straight channel, we derive a universal scaling relationship between the Sherwood and Bejan numbers, i.e. the dimensionless permeate flux through the membrane and the pressure drop along the channel, respectively, and generalize this result to membranes subject to morphological and/or topological modifications, i.e. whose shape (wiggliness) or surface roughness is altered from the rectangular and flat reference case. We demonstrate that a universal scaling can be identified through the definition of a modified Reynolds number, $Re^{\star}$, that accounts for the additional length scales introduced by the membrane modifications, and a membrane performance index, ξ, an aggregate efficiency measure with respect to both clean permeate flux and energy input required to operate the system. Our numerical simulations demonstrate that 'wiggly' membranes outperform 'rough' membranes for smaller values of $Re^{\star}$, while the trend is reversed at higher $Re^{\star}$. The proposed approach is able to quantitatively investigate, optimize and guide the design of both morphologically and topologically altered membranes under the same framework, while providing insights into the physical mechanisms controlling the overall system performance.

Key words: membranes, porous media

1. Introduction

Reverse osmosis membrane (ROM) filtration systems are utilized in wastewater recovery (Benito & Ruiz 2002; Cath *et al.* 2005; Rahardianto, McCool & Cohen 2008; Shannon *et al.* 2008; Greenlee *et al.* 2009; McCool *et al.* 2010; Rahardianto, McCool & Cohen 2010), seawater desalination (Fritzmann *et al.* 2007; Elimelech & Phillip 2011; Matin *et al.* 2011), landfill water treatment (Peters 1998; Chianese, Ranauro & Verdone 1999), etc. Typically, ROMs perform one of the final stages

† Email address for correspondence: ibattiat@stanford.edu

of water treatment and are designed to filter ions or soluble substances. Bio-active films (Bucs *et al.* 2016) and porous materials (Shih *et al.* 2005; Rahardianto *et al.* 2006) are two of the media frequently used as separation membranes. The selective membrane only allows de-mineralized/deionized water to penetrate, and forms a physical boundary between the purified water flux (i.e. the permeate flux), collected on the draw side of the membrane, and the pre-treatment (feed) water. High pressure is applied and maintained on the concentrated (feed) side to drive the permeate flux of treated water. As with any filtration process, ROM performance is largely impacted by fouling. The filtered solute (mineral or ion) accumulates on the membrane surface by creating a blockage. Fouling is the primary process affecting filtration performance since it (i) reduces the clean water permeate flux and (ii) increases the energy (i.e. the driving pressure drop) required to generate a unitary permeate flux. Optimization of filtration systems has primarily focused on maximizing membrane permeability and selectivity, while minimizing the reduction of permeate induced by fouling. However, it is critical to consider factors other than permeability and selectivity in materials design (Park *et al.* 2017).

While the type of foulant greatly depends on solute and membrane properties, its impact on ROM performance and operation costs is similar. In bio-active membranes, microbial growth is the primary cause of fouling (Bucs *et al.* 2016). Instead, perm-selectivity of porous ROM membranes to the solvent (e.g. clean water) leads to a localized increase of solute concentration on the feed side, also known as concentration polarization (CP) (Brian 1965; Jonsson & Boesen 1977; Sablani *et al.* 2001; Kim & Hoek 2005; McCutcheon & Elimelech 2006). CP refers to the rise of concentration relative to the bulk concentration at a membrane surface and it is due to the rejection of solute by membrane selectivity. Quoting from Lyster & Cohen (2007), the 'rejection of salt ions at a membrane surface in cross-flow reverse osmosis results in increased solute concentration near the membrane surface (i.e. concentration polarization)'. As a result, solute precipitates from the solution and accumulates or crystallizes on the membrane surface (Shih *et al.* 2005; Rahardianto *et al.* 2006).

Beside surface chemistry, the fouling propensity of a membrane depends greatly on its surface topological properties, such as roughness, and its morphology (or shape). Literature and experience show that modification of membrane surfaces with chemical coatings can be effective but not sufficient for controlling membrane fouling. The discovery that sub-micron patterning of a membrane surface can improve its fouling resistance provides an orthogonal membrane design parameter (Maruf *et al.* 2013*a*,*b*, 2014). As a result, different mechanisms at vastly different scales have been proposed to control fouling (Zhang *et al.* 2016): (i) modifications of membrane/separator morphology at the system scale ($\sim$cm) (Ma & Song 2006; Guillen & Hoek 2009; Suwarno *et al.* 2012; Xie, Murdoch & Ladner 2014; Sanaei & Cummings 2017); (ii) modifications of the membrane topology at the micro-scale ($\sim$mm $-$ μm) (Elimelech *et al.* 1997; Bowen & Doneva 2000; Vrijenhoek, Hong & Elimelech 2001; Kang *et al.* 2007*a*; Ba, Ladner & Economy 2010; Battiato, Bandaru & Tartakovsky 2010; Ladner *et al.* 2012; Maruf *et al.* 2013*a*,*b*, 2014; Battiato 2014; Ling, Tartakovsky & Battiato 2016); and (iii) chemical or surface treatment to alter the interaction force between the membrane and the foulant at the nano-scale ($\sim$nm) (Kang *et al.* 2007*b*; Sanaei *et al.* 2016).

Attempts to control fouling in ROM commercial systems have been primarily limited to the inclusion of spacers transverse to the main flow direction. These have shown limited success since they fail to sufficiently perturb the flow field in the proximity of the membrane boundary, where fouling is localized. Furthermore,

spacers increase the flow resistance, i.e. the energy input to sustain a given pressure drop. More promising has been the use of micro/nano-patterns embossed above the membrane. These are able to more effectively perturb the flow locally, and only mildly impact the overall dissipation of the system. Surface treatment can effectively modify interaction properties, for instance wettability, roughness and molecular attraction between the membrane and the foulant, however such modifications generally undergo irreversible degradation during filtration.

Despite the fact that a number of studies have experimentally or analytically demonstrated the impact of morphological and topological alteration on, e.g. solute dispersion and fouling at the system (macro-) scale (Battiato *et al.* 2010; Griffiths, Howell & Shipley 2013; Maruf *et al.* 2013*b*; Battiato & Rubol 2014; Ling *et al.* 2016, 2018; Rubol, Battiato & de Barros 2016; Rubol, Ling & Battiato 2018), ROM systems are still primarily optimized by trial and error. This is due to the lack of quantitative understanding of the impact of morphological and/or topological modifications on membrane fouling at prescribed operating conditions. While (semi-)analytical methods can provide general guiding principles and basic process understanding for highly idealized systems (Kang *et al.* 2007*b*; Battiato 2012; Ling *et al.* 2016; Sanaei *et al.* 2016; Sanaei & Cummings 2017), their direct applicability to the optimization and design of real systems is questionable. On the other hand, laboratory experimentation of promising designs, and their consequent optimization, may be prohibitively expensive. A number of two-dimensional (2-D) and 3-D numerical simulators have been developed to study fouling (Bhattacharyya *et al.* 1990; Lyster & Cohen 2007; Park & Kim 2013; Bucs *et al.* 2014, 2016; Xie *et al.* 2014; Kang *et al.* 2017). Yet, they generally do not account for unsteady effects and the coupling between hydrodynamics and membrane fouling, which dynamically alters the permeate flux distribution, i.e. the boundary condition for the flow field (Lyster & Cohen 2007). The flow field is influenced by the local blockage of the membrane, which further impacts the distribution of the solute in the bulk, its CP and, finally, fouling formation. A number of models have been proposed to represent different mechanisms leading to fouling (e.g. standard and complete blocking, cake filtration, etc.), and their impacts on system scale performance, quantified by, e.g. energy input and permeate flux (Griffith, Kumar & Stewart 2014; Griffith, Kumar & Stuart 2016; Sanaei & Cummings 2017). However, the fouling mechanism is generally not dynamically coupled to the local hydrodynamics, and its dynamic feedback on flux reduction is not accounted for. Attempts to incorporate unsteady effects included the definition of time-dependent absorption functions to model fouling growth (Bucs *et al.* 2014, 2016): although the growth function is time dependent, the governing equations for flow and transport remain at the steady state. An explicit treatment of the dynamic coupling between bulk transport, surface fouling and hydrodynamics is necessary to elucidate the mechanisms that control (i) the onset of fouling, (ii) the development of a stable fouling pattern and (iii) the dynamic flux reduction as a result of clogging.

In this work, we develop a three-dimensional model and computational framework to study fouling spatio-temporal evolution which captures (i) the two-way coupling between bulk concentration, flow velocity and foulant accumulation on the membrane surface, (ii) the relationship between CP close to the membrane surface and fouling on the membrane and (iii) the initiation and development of the foulant spatial pattern. Such a framework allows us to quantitatively investigate the impact of surface topology (i.e. roughness) and morphology (i.e. wiggliness, shape) on fouling, and to identify dynamical conditions under which such alterations are warranted. Here, we intend to lay out the foundations of a mathematical framework to address some of the open questions outlined by Park *et al.* (2017), who state that

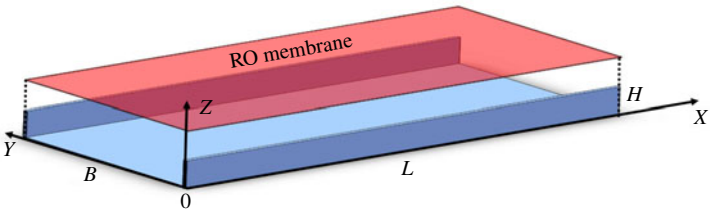

FIGURE 1. (Colour online) Three-dimensional sketch of the computational domain (exploded-view), where the red boundary represents the ROM and the blue boundaries are the flow channel walls.

> 'there is a real need for fundamental modeling, at length scales ranging from atomistic to continuum, to provide rational guidance for designing future membranes. [...] In all cases, better understanding of structure-property-performance relationships in new, as well as existing, membrane materials is urgently needed'.

The paper is organized as follows. In § 2, we introduce the model in dimensional (§ 2.1) and dimensionless (§ 2.2) form, and derive universal scaling laws in the long time limit for a rectangular flat membrane (§ 2.3). In § 3, we first perform a convergence study (§ 3.1) and then validate the model against unsteady permeate flux measurements and steady-state fouling patterns (§ 3.2). Section 4 investigates the impact of morphological and topological modifications of the membrane shape (i.e. wiggliness) and surface (i.e. roughness) on both foulant accumulation, clean water permeate flux and operating pressure drop. We focus on 18 membrane designs which include 9 purely morphological (M-), 6 purely topological (T-) and 3 hybrid (H-) designs which include both topological and morphological modifications (§ 4.1). We then introduce new scaling variables (§ 4.2) and derive scaling laws (§ 4.3) valid for all designs. We finally show how the previous framework can be used for membrane shape and surface optimization (§ 4.4). We provide concluding remarks in § 5.

2. Model

2.1. *Governing equations*

We consider a pressure-driven flow in a channel of length L and rectangular cross-section (in the (Y, Z)-plane) whose top side, located at $Z = H$, consists of a flat ROM lying in the (X, Y)-plane, parallel to the mean flow. The clean water is cross-filtered from the feed solution, conveyed to the membrane through the flow channel, as the membrane is permeable to water molecules only and impermeable to the solute dissolved in the feed. The concentrated solution (feed) enters the channel from the inlet section located at $X = 0$ and exits the domain at $X = L$. Solute rejection by the membrane (aka membrane perm-selectivity) leads to the emergence of local solute concentration gradients in the feed at the membrane/solution interface and to subsequent accumulation of foulant on the membrane, in the interior of the computational domain ($0 < Z \leqslant H$). A schematic of the domain is shown in figure 1.

We focus on fouling accumulation as a function of both time and space. The filtration process is described by a set of coupled transient equations for the velocity field $\boldsymbol{U}$, the bulk concentration C_b of solute within the feed solution and the foulant

surface concentration C_s on the ROM. The flow field $\boldsymbol{U}(\boldsymbol{X}, T) = (U, V, W)$ satisfies the transient incompressible Navier–Stokes and continuity equations

$$\frac{\partial \boldsymbol{U}}{\partial T} + (\boldsymbol{U}\cdot\boldsymbol{\nabla})\boldsymbol{U} + \boldsymbol{\nabla}\hat{P} = \boldsymbol{\nabla}\cdot(\nu\boldsymbol{\nabla}\boldsymbol{U}), \tag{2.1a}$$

$$\boldsymbol{\nabla}\cdot\boldsymbol{U} = 0, \tag{2.1b}$$

where $\hat{P}$ $[L^2T^{-2}]$ is a rescaled pressure and is defined as

$$\hat{P} = \frac{P^\star}{\rho}, \tag{2.2}$$

with $P^\star$ fluid pressure, and ν and ρ the kinematic viscosity and density of the bulk solution, respectively. Gravitational effects are neglected. Equations (2.1) are subject to inlet, outlet, cross-flow velocity and no-slip boundary conditions at the inlet, outlet, on the ROM and the three impermeable walls, respectively,

$$\boldsymbol{U} = (U_{in}, 0, 0), \quad \boldsymbol{n}\cdot\boldsymbol{\nabla}\hat{P} = 0 \quad \text{for} \quad \boldsymbol{X} = (0, Y, Z), \tag{2.3a}$$

$$\boldsymbol{n}\cdot\boldsymbol{\nabla}\boldsymbol{U} = 0, \quad \hat{P} = P_{out} \quad \text{for} \quad \boldsymbol{X} = (L, Y, Z), \tag{2.3b}$$

$$\boldsymbol{U} = (0, 0, W_H), \quad \boldsymbol{n}\cdot\boldsymbol{\nabla}\hat{P} = 0 \quad \text{for} \quad \boldsymbol{X} = (X, Y, H), \tag{2.3c}$$

$$\boldsymbol{U} = (0, 0, 0), \quad \boldsymbol{n}\cdot\boldsymbol{\nabla}\hat{P} = 0 \quad \text{for} \quad Y = \{0, B\}, \quad \text{or} \quad Z = 0, \tag{2.3d}$$

where W_H is the local permeate flux through the membrane. It is defined as the difference between W_m, the clean water flux, i.e. the membrane flux in absence of fouling, and W_f, the flux reduction due to foulant accumulation, i.e.

$$W_H = W_m - W_f. \tag{2.4}$$

In (2.4), W_m and W_f are defined as follows

$$W_m = \frac{k_m}{\nu B}\delta\hat{P}, \tag{2.5}$$

with k_m [mD $= 9.869 \times 10^{-16}$ m^2] the membrane permeability, and $\delta\hat{P}$ the local pressure head drop across the membrane,

$$\delta\hat{P} = \hat{P}(X, Y, Z = H^-) - P_{amb}, \tag{2.6}$$

where $P_{amb} = 0$ is the ambient pressure. Although various methods have been proposed to model the flux reduction W_f due to fouling, two approaches are generally used: the flux reduction is represented either (i) as a function of the CP (or concentration in close proximity of the membrane surface) (Lee, Baker & Lonsdale 1981; Lyster & Cohen 2007; Sagiv *et al.* 2014), or (ii) by postulating a functional relationship between the foulant and membrane resistance (Griffiths *et al.* 2013; Sanaei *et al.* 2016; Sanaei & Cummings 2017). The first approach is based on the assumption that the fouling and CP have the same (or similar) impact on the flow field. However, unlike CP, which vanishes when pressure is released, some foulant may irreversibly precipitate on the membrane (Shih *et al.* 2005; Xie *et al.* 2014). The second approach is based on modelling the foulant as an additional resistance to the membrane: in such models, the relationship between foulant-induced resistance and flux reduction contains parameters (e.g. permeability of the foulant or the attraction coefficient) that

are often difficult to experimentally determine (Sanaei & Cummings 2017; Takatori & Brady 2017; Sanei & Cummings 2018).

In this work, instead we model flux reduction due to foulant accumulation as

$$W_f = A_f(C_s - C_b), \tag{2.7}$$

where A_f is a constant, and C_s and C_b are the foulant dimensionless surface and bulk concentrations defined as

$$C_s = \frac{\hat{C}_s}{C_0 \cdot B}, \tag{2.8}$$

and

$$C_b = \frac{\hat{C}_b}{C_0}, \tag{2.9}$$

where $\hat{C}_s$ [mol m^{-2}] and $\hat{C}_b$ [mol m^{-3}] are the corresponding dimensional concentrations, and C_0 is the reference bulk concentration (usually taken as the inlet concentration). Equation (2.7) hypothesizes that the reduced flux is proportional to the amount of locally precipitated (or deposited) foulant, where the local accumulation of the foulant scales with the rate of precipitation. As a result, the proposed relationship relates permeate flux loss with the precipitation rate and directly links/couples the three critical quantities governing the feedback between local hydrodynamics (W_f, or $\boldsymbol{U}$), bulk solute transport (C_b) and foulant accumulation (C_s). The relationship, which will be subject to validation against experimental data in § 3, has the following advantages: (i) it disentangles CP from fouling, (ii) its parameter A_f can be calibrated using experimental measurements, as outlined in § 3.2, and (iii) it relates quantities that can be independently measured in experiments; as a consequence, the validity of such a postulated relationship can be immediately tested and/or generalized, if necessary. The expression $A_f(C_s - C_b)^n$ is widely used for studying crystallization kinetics (Brusilovsky, Borden & Hasson 1992; Lee & Lee 2000; Cetin, Eroğlu & Özkar 2001; Sheikholeslami & Ong 2003; Shih *et al.* 2005), similar to those occurring for certain foulants, e.g. gypsum, with an exponent n ranging between 1 and 2. If we normalize the constant A_f by the membrane permeability, and define

$$\hat{A}_0 = \frac{A_f}{k_m/(\nu B)}, \tag{2.10}$$

then (2.4) can be written as

$$W_H|_{Z=H} = \frac{k_m}{\nu B}[\delta\hat{P} - \hat{A}_0(C_s - C_b)], \tag{2.11}$$

which describes how fouling affects the decrease in permeate flux dynamically: as the foulant surface concentration, C_s, increases, the local permeate velocity W_H and flux will dynamically decrease. In this context, $\hat{A}_0(C_s - C_b)$ can be thought of as a loss of effective pressure drop across the membrane due to foulant deposition. We emphasize that the boundary condition (2.11) allows one to (i) distinguish CP from foulant accumulation, (ii) fully couple the flow field, concentration field and the foulant deposition while capturing its effect on permeate flux dynamically and (iii) link flux reduction with foulant accumulation/precipitation on the membrane.

The solute bulk concentration C_b satisfies a classic advection–diffusion equation

$$\frac{\partial C_b}{\partial T} + \boldsymbol{u} \cdot \boldsymbol{\nabla} C_b - D\nabla^2 C_b = 0, \tag{2.12}$$

subject to a flux balancing boundary condition on the ROM (Lyster & Cohen 2007)

$$D\frac{\partial C_b}{\partial Z} = R_i W_H C_b \quad \text{at } Z = H, \tag{2.13}$$

where D is the molecular diffusion coefficient of the bulk solute, W_H is given by (2.11) and R_i is the intrinsic membrane rejection rate (Lyster & Cohen 2007). In this study, we set $R_i = 100\,\%$. Furthermore, equation (2.12) is subject to no-flux boundary conditions at the outlet and on the channel solid walls, i.e. $\boldsymbol{n} \cdot \boldsymbol{\nabla} C_b = 0$ at $Z = 0$, $Y = \{0, H\}$ and $X = L$, and a Dirichlet boundary condition at the inlet, $C_b = 1$ at $X = 0$. The surface concentration of the foulant C_s satisfies a transient adsorption–desorption equation (Jones & O'Melia 2000).

$$\frac{\partial C_s}{\partial T} = K_1 \cdot (C_{s,max} - C_s) \cdot C_b - K_2 C_s, \tag{2.14}$$

where K_1, K_2 and $C_{s,max}$ are the adsorption and desorption coefficients and the equilibrium foulant concentration, respectively. All equations are coupled through the boundary conditions defined on the membrane.

The set of (2.1)–(2.14) allows us to solve for the dynamical evolution of fouling by coupling the transient equations (2.1), (2.12) and (2.14) through the boundary conditions (2.11) and (2.13). We emphasize that the proposed model of flux reduction, equation (2.7), dynamically captures the two-way coupling between hydrodynamics, bulk transport and fouling. The primary advantages of the model are the following: (i) all physics is resolved dynamically; (ii) by imposing the condition that $C_{s,max} > C_b$, the growth function (2.14) guarantees the that $A_f(C_s - C_b) > 0$, and prevents any unphysical flux increase; (iii) the coupling between bulk and foulant concentration, and between the foulant and flux reduction is explicitly modelled and no additional hypothesis is needed to describe the functional dependence between foulant accumulation and membrane resistance (Griffiths *et al.* 2013; Sanaei *et al.* 2016; Sanaei & Cummings 2017); (iv) different growth kinetics can be accounted for by appropriately modifying K_1 and K_2, for instance, soluble foulant (e.g. sodium chloride) has $K_1 > 0$ and $K_2 > 0$, while more resilient foulant (e.g. calcium carbonate) has $K_1 > 0$ and $K_2 \approx 0$. It is worth emphasizing that the model parameters are either intrinsic properties of the membrane (e.g. R_i and k_m) or can be measured from experiments when the solution–membrane pair is given. For instance, K_1 and K_2 can be determined experimentally as discussed by Jones & O'Melia (2000). To summarize, the novelty of the proposed model lies primarily in the formulation of the flux (2.7), and in its ability to capture the two-way dynamic coupling between $\boldsymbol{U}$, C_b and C_s.

Once the foulant surface concentration $C_s(X, Y, H, T)$ is determined, the non-fouled regions Γ_n on the ROM are identified by locally thresholding C_s, i.e.

$$\Gamma_n(T) := \{(X(T), Y(T), H) | C_s \leqslant \alpha C_{s,max}\}, \quad \text{where } \alpha \in [0, 1],\ T \in (0, T_{max}), \tag{2.15}$$

which represents the area formed by a set of membrane points (X, Y, H) that satisfy the condition $C_s \leqslant \alpha C_{s,max}$. In this study we set $\alpha = 1$. The unit permeate flux Q_m $[LT^{-1}]$ is

$$Q_m(T) = \frac{1}{A_m} \int_{\Gamma_n(T)} W_H(X, Y, T)\, \mathrm{d}\mathcal{A}, \tag{2.16}$$

where A_m is the total surface of the membrane.

2.2. *Dimensionless formulation*

We start by defining the Sherwood number, i.e. the ratio between the convective and diffusive mass transport toward the membrane or the dimensionless permeate flux,

$$Sh = \frac{Q_{m,\infty} B}{D}, \tag{2.17}$$

where $Q_{m,\infty}$ is the steady-state permeate flux, and the Bejan number, i.e. the dimensionless pressure head drop along the channel,

$$Be = \frac{B^2}{\nu^2} \Delta \hat{P}, \tag{2.18}$$

where $\Delta \hat{P} = \hat{P}_{in} - \hat{P}_{out}$ is the modified pressure drop along the membrane between the inlet ($X = 0$) and the outlet ($X = L$). Furthermore, we define the following dimensionless quantities,

$$\boldsymbol{u} = \frac{\boldsymbol{U}}{U_{in}}, \quad \boldsymbol{x} = \frac{\boldsymbol{X}}{B}, \quad t = \frac{T}{B/U_{in}}, \quad P = \frac{\hat{P}}{\nu^2/B^2}, \quad A_0 = \frac{\hat{A}_0}{\nu^2/B^2}, \quad w_h = \frac{W_H}{U_{in}}, \quad h = \frac{H}{B}, \tag{2.19a–g}$$

where $\boldsymbol{u} = (u, v, w)$ and $\boldsymbol{x} = (x, y, z)$ are the dimensionless velocity field and coordinate axes. We also introduce the dimensionless numbers

$$Re = \frac{U_{in} B}{\nu}, \quad Pe = \frac{U_{in} B}{D}, \quad Dc = \frac{k_m}{B^2}, \quad Da_I = K_1 \frac{B}{U_{in}}, \quad Da_{II} = K_2 \frac{B}{U_{in}}, \tag{2.20a–e}$$

where Re, Pe, Dc, Da_I and Da_{II} are the Reynolds, Péclet, Darcy and Damköhler numbers related to the adsorption and desorption reactions, respectively. Then, the transport equations (2.12) and (2.14) for the bulk and surface concentration, C_b and C_s, can be cast in dimensionless form

$$Pe \left(\frac{\partial C_b}{\partial t} + \boldsymbol{u} \cdot \boldsymbol{\nabla} C_b \right) - \nabla^2 C_b = 0, \tag{2.21}$$

and

$$\frac{\partial C_s}{\partial t} = Da_I (C_{s,max} - C_s) C_b - Da_{II} C_s, \tag{2.22}$$

subject to

$$\frac{\partial C_b}{\partial z} = Pe\, w_h C_b, \tag{2.23a}$$

$$w_h = \frac{Dc}{Re} \left[\delta P - A_0 \left(C_s - C_b \right) \right], \tag{2.23b}$$

on the membrane surface ($z = h$). For practical applications, it is often important to identify the relationship between pressure drop and the permeate flux when the system reaches equilibrium in the long-time limit, i.e.

$$Sh = \Pi (Be, Re, Pe, Dc, \text{etc.}), \tag{2.24}$$

using the formulation above. In the following section, we will derive an analytical scaling behaviour between Be and Sh.

2.3. Long-time scaling limit

At steady state, equation (2.22) reads

$$0 = Da_I(C_{s,max} - C_s)C_b - Da_{II}C_s, \tag{2.25}$$

namely,

$$C_s = \frac{Da_I C_{s,max} C_b}{Da_{II} + Da_I C_b}. \tag{2.26}$$

Combining (2.26) with the membrane permeate flux equation (2.23*b*), we obtain

$$w_h = \frac{Dc}{Re}\left[\delta P - A_0\left(\frac{Da_I C_{s,max} C_b}{Da_{II} + Da_I C_b} - C_b\right)\right]. \tag{2.27}$$

Assuming the foulant accumulates much faster than it dissolves, i.e. $Da_I C_b/Da_{II} \ll 1$, equation (2.27) can be simplified as follows

$$w_h = \frac{Dc}{Re}[\delta P - A_0(C_{s,max} - C_b)]. \tag{2.28}$$

Also, under the assumption that at steady state $P(z = h^-) \sim P_{in}$, while accounting for (2.18), equation (2.6) can be written as

$$\delta P = Be + P_{out}, \tag{2.29}$$

where P_{in} and P_{out} are the dimensionless inlet and outlet pressures. Inserting (2.29) into (2.28), we obtain

$$w_h = \frac{Dc}{Re}[Be + P_{out} - A_0(C_{s,max} - C_b)]. \tag{2.30}$$

Under the hypothesis that $C_b \approx C_b(Z)$, i.e. the variation of the bulk concentration C_b with x and y is negligible, while accounting for (2.30), the boundary condition (2.23*a*) can be written as

$$C_b' = \Pi_I C_b^2 + \Pi_{II} C_b, \tag{2.31}$$

where

$$\Pi_I = Dc\, Sc\, A_0, \tag{2.32a}$$

$$\Pi_{II} = Dc\, Sc(Be - Be^\star), \tag{2.32b}$$

and

$$Be^\star = A_0 C_{s,max} - P_{out}, \tag{2.33}$$

since $Sc = Pe/Re = \nu/D$. Equation (2.31) is a homogeneous nonlinear ordinary differential equation for C_b, which can be solved by using the following substitution:

$$\gamma = \frac{1}{C_b}. \tag{2.34}$$

The transformed equation gives us a non-homogeneous equation for γ

$$-\gamma' = \Pi_I + \Pi_{II}\gamma, \tag{2.35}$$

whose solution, $\gamma = \gamma_h + \gamma_p$, is given by the general and particular solutions, γ_h and γ_p, which satisfy

$$-\gamma_h' = \gamma_h \Pi_{II}, \tag{2.36}$$

and

$$-\gamma_p' = \Pi_I + \gamma_p \Pi_{II}, \tag{2.37}$$

respectively. The solution is

$$\gamma = \gamma_h + \gamma_p = C_1 \exp(-\Pi_{II} z) - \frac{\Pi_I}{\Pi_{II}}, \tag{2.38}$$

where C_1 is determined by imposing the boundary condition

$$C_b = 1, \quad \text{when } z = 0, \tag{2.39}$$

i.e. the channel bottom reaches saturation at steady state. The solution reads

$$C_b = \frac{\Pi_{II}}{(\Pi_I + \Pi_{II}) + \exp(-\Pi_{II} h) - \Pi_I}. \tag{2.40}$$

Additionally, we assume that at steady state $w_h = Q_{m,\infty}/U_{in}$, i.e.

$$w_h = \frac{1}{Pe} Sh. \tag{2.41}$$

Combining (2.41) with (2.30), we obtain

$$Sh = \Pi_I C_b + \Pi_{II}. \tag{2.42}$$

Evaluating C_b at the membrane surface, $z = h$, while accounting (2.40), leads to

$$Sh = \Pi_{II} - \frac{\Pi_{II}}{1 - \left(\dfrac{\Pi_{II}}{\Pi_I} + 1\right) - \exp\left(-\Pi_{II} h\right)}. \tag{2.43}$$

Substituting (2.32*b*), we obtain

$$Sh = Dc\, Sc(Be - Be^\star) \left\{ 1 - \frac{1}{1 - \left[1 + \dfrac{1}{\Pi_I}(Be - Be^\star)\right] \exp\left[-hDc\, Sc(Be - Be^\star)\right]} \right\}, \tag{2.44}$$

which provides the relationship between the dimensionless permeate flux, *Sh*, and the dimensionless pressure drop, *Be*. It is worth emphasizing that, at steady state, *Sh* can be written as a function of only Bejan number *Be*, Darcy number, *Dc*, i.e. the dimensionless permeability of the membrane, and Schmidt number *Sc* (as well as the geometric parameter *h*), while it is independent of *Re*, *Pe* and *Da*. However, since *Be* is certainly function of *Re* (as *Sh* is), (2.44) implies that both *Sh* and *Be* exhibit the same scaling behaviour in terms of Reynolds number.

We now look at the asymptotic behaviour of (2.44) for $Be \to 0$ and $Be \to \infty$, while keeping all the other dimensionless parameters constant, and obtain

$$\lim_{Be \to 0} Sh \sim \text{const}, \tag{2.45a}$$

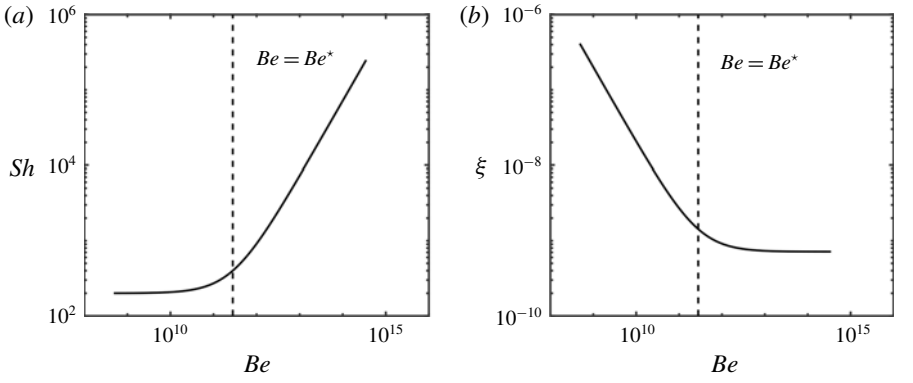

FIGURE 2. (*a*) Analytical solution of Sherwood number *Sh* as a function of Bejan number *Be* for parameter values listed in table 1; (*b*) analytical solution of the efficiency ξ as a function of Bejan number.

$$\lim_{Be\to\infty} Sh \sim Be, \tag{2.45b}$$

with the transition between the two scaling behaviours occurring at

$$Be \sim Be^\star. \tag{2.46}$$

Since *Be* can be associated with the energy input for filtration operations and *Sh* is the quantity to maximize, we define the overall filtration performance index, ξ, as:

$$\xi = \frac{Sh}{Be}, \tag{2.47}$$

where the higher the value of ξ, the higher the membrane efficiency both in terms of permeate flux and energy input. Combining (2.47) with (2.45*a*) and (2.45*b*), one obtains

$$\xi \sim \frac{1}{Be}, \quad Be \to 0, \tag{2.48}$$

and

$$\xi \sim \text{const } Be \to \infty, \tag{2.49}$$

respectively. Figure 2(*a*,*b*) shows the relationship between the Sherwood and the Bejan numbers as defined by (2.44) for the set of parameters listed in table 1, and the membrane performance index ξ, respectively. The dashed line is the transition $Be = Be^\star$ between the two scaling behaviours. The scalings (2.45)–(2.49) suggest that an increase in the inlet velocity (or, equivalently, pressure drop) leads to an increase in the permeate flux after a certain threshold ($Be^\star$) is overcome. However, the overall system performance drops as a result and reaches a plateau when $Be \to \infty$: at high flow rates, the increased energy requirement to sustain a given pressure drop outweighs any benefits due to reduced fouling. This suggests (and will be confirmed in the following) that under these conditions, surface topology modifications may better impact membrane performance than morphological changes (e.g. the adoption of spacers). Instead, when $Be \to 0$, *Sh* does not depend strongly on the pressure drop.

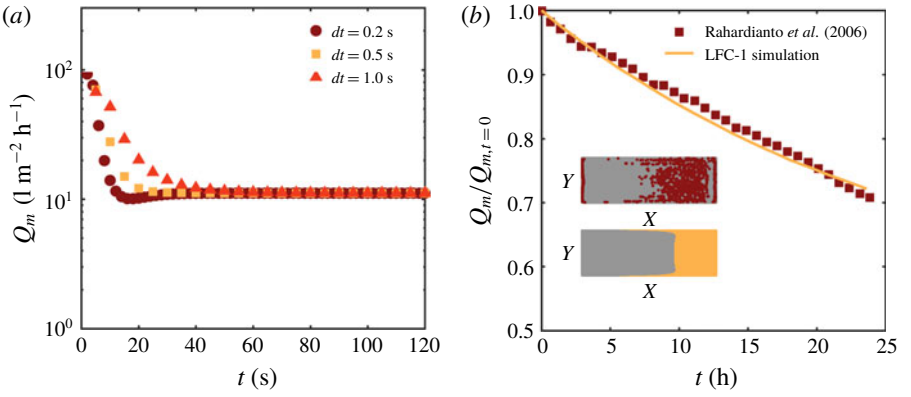

FIGURE 3. (Colour online) (*a*) Simulated permeate flux for different time steps. Results show that the steady-state solution is reached around $T \approx 60$ s; (*b*) Comparison between dynamic measurements of permeate flux collected by Rahardianto *et al.* (2006) (symbols) and simulated permeate flux decrease (solid line). The inset shows a comparison between the digitalized experimental steady-state fouling pattern (top) and the simulated one (bottom).

While the scaling behaviour (2.48) and (2.49) is obtained for the benchmark case of a rectangular membrane, in the following we move forward by, first, validating the proposed model equations against experimental results on fouled rectangular membranes (§ 3), and then generalize the approach to membranes with complex morphological and topological features (i.e. additional length scales) (§ 4).

3. Numerical model validation

In the following, we proceed by validating (i) the model (2.1)–(2.14) against experimental data and (ii) the scaling relationships between the quantities of interest.

3.1. *Implementation and convergence study*

We implement (2.1)–(2.14) in the finite-volume OpenFOAM® framework, by developing the customized solver SUMs (Stanford University Membrane solver). The solver is explicit in time and second order in space. A convergence study is performed using a straight channel of dimensions $H \times L \times B = 2 \times 70 \times 5$ mm^3. The permeate flux across the membrane $Q_m(T)$ (l m^{-2} h^{-1}) is calculated using three different time steps $dT = \{0.2, 0.5, 1.0\}$ s, and simulated for $T_{max} = 120$ s. Figure 3 shows the calculated $Q_m(T)$ for the three different scenarios. The three transient simulations converge to the same steady state, independently of the time step. The steady-state solution is achieved at $T \approx 60$ s. For simulations involving non-rectangular geometries, we run the simulations for 400 s to ensure steady state is reached. In the next section, we proceed with validating the code against fouling experiments.

3.2. *Experimental validation*

To validate the model proposed in § 2 and the developed solver, we compare numerical simulations of permeate flux decrease over time and fouling development with membrane fouling experiments conducted by Rahardianto *et al.* (2006). In

Parameters	U_{in} (m s^{-1})	Re (−)	$Re^{\star}$ ($\times 10^3$)	k_m (mD)	K_1 (s^{-1})	K_2 (s^{-1})	$C_{s,max}$ (−)	$\hat{P}_{out}$ (m^2 s^{-2})	$\hat{A}_0$ (m^2 s^{-2})
Rahardianto *et al.*	0.15	500	—	6.95	—	—	—	1000	—
LFC - 1 Simulation	0.15	500	—	6.95	1×10^{-5}	1×10^{-7}	2	1000	100
SIM - 1	0.05	250	0.25–3	7.00	0.1	0.001	2	1000	100
SIM - 2	0.075	375	0.38–5						
SIM - 3	0.1	500	0.5–7						
SIM - 4	0.15	750	0.75–10						
SIM - 5	0.175	875	0.87–13						
SIM - 6	0.2	1000	10–15						

TABLE 1. Parameters of all numerical simulations. First row: parameters from the experimental study on low fouling composite (LFC) membranes by Rahardianto *et al.* (2006); second row: parameters of the numerically simulated experiment by Rahardianto *et al.* (2006). Other rows: parameters of the synthetic examples (SIM - 1 to SIM - 6) of § 4 with Darcy number $Dc = 1.967 \times 10^{-10}$ and Schmidt number $Sc = 500$.

Rahardianto *et al.*'s (2006) study, fouling experiments are performed using a low fouling composite (LFC) membrane with crystallized gypsum as the foulant. Both steady-state and transient measurements of permeate flux, as well as final fouling patterns, are provided. In the following, we use the time-varying permeate flux measurements and the final fouled membrane image reported by Rahardianto *et al.* (2006) as the benchmark.

The simulation parameters are set to match the experimental set-up and operating conditions. Table 1 lists all the experimental parameters used in the simulation. Since measurements of the membrane permeability are not provided, k_m is estimated from the pressure and flux measured during a clean water experiment through (2.11), where C_b and C_s are set to zero. The coefficient A_0 is fitted to match the steady-state flux at $T \to \infty$, $Q_m(T = \infty)$.

The coefficients K_1, K_2 and $C_{s,max}$ in (2.14), not provided by Rahardianto *et al.* (2006), are estimated as follows: following the experimental observations by Xie *et al.* (2014) where foulant accumulated on the membrane is approximately $C_{s,max} = 1.44C_0$ (i.e. 2–4 times the bulk concentration) for $C_0 = 0.4$–0.6 M, we set the equilibrium foulant concentration to $C_{s,max} = 2C_0$. The membrane adsorption/desorption rate θ, i.e. the ratio between K_2 and K_1, $\theta := K_2/K_1$ varies from 0.1 to 0.001 (Jones & O'Melia 2000). In our study, we set $\theta = 0.01$, with $K_1 = 1 \times 10^{-5}$ and $K_2 = 1 \times 10^{-7}$.

Figure 3(*b*) shows the comparison between the numerical predictions and the experimental measurements of the permeate flux decline as a function of time. The measured and predicted foulant spatial patterns are shown in the inset of figure 3(*b*). The comparison demonstrates that the system (2.1)–(2.14) can correctly capture both unsteady effects as well as the spatio-temporal evolution of foulant accumulation.

In the following, we perform a series of unsteady fully 3-D numerical studies to assess and elucidate the impact that different modifications of the filtration system have on fouling. We classify them into two broad classes: (i) morphological changes entail modifications of the design of the flow channel (i.e. the spacer morphology) and have characteristic length scales of the order of mm; instead, (ii) topological alterations introduce micro-scale patterns/features on the membrane surface and have characteristic length scales (μm or sub-μm) that are much smaller than the channel dimensions.

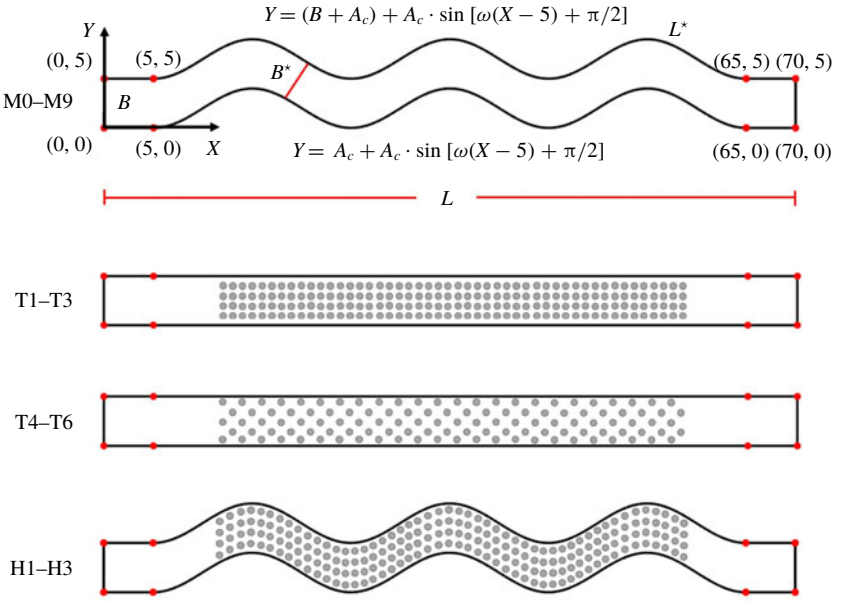

FIGURE 4. (Colour online) Schematic of the channel geometries investigated. Designs M0–M9 involve morphological changes (i.e. various sinusoidal shapes); designs T1–T6 involve topological changes where the membrane is patterned with pillars of different heights and arrangements; H1–H3 are hybrid designs which combine both morphological and topological alteration of the membrane.

4. Impact of membrane morphology and topology on fouling control

In this section, we use the validated simulator to perform a number of numerical experiments. Our goals are to (i) examine the validity of the analytical expression (2.44) derived in § 2.3, (ii) elucidate the correlation between local hydrodynamics, CP and fouling, (iii) study the transient behaviour of foulant accumulation and (iv) develop a scaling analysis/framework at the system level able to capture both morphological and topological modifications of the membrane for performance optimization.

4.1. *Numerical simulations*

We study 18 membrane designs: 9 purely morphological (M1 to M9), 6 purely topological (T1 to T6) and 3 hybrid designs (H7 to H9) which include both topological and morphological modifications (see figure 4). The fully three-dimensional domains contain 500 000–1 000 000 finite-volume cells, depending on the domain geometry, with a density of 10 cells per unit length. A smooth straight channel design (M0) is modelled as the reference case. The morphology of choice in this study is sinusoidal channels of different periods and amplitudes (Xie *et al.* 2014). For the designs M1–M9, the membrane shape is defined by the following bottom and top boundaries in the (X, Y)-plane,

$$Y = (A_c + B) + A_c \sin[\omega(X - B) + \pi/2], \tag{4.1a}$$

$$Y = A_c + A_c \sin[\omega(X - B) + \pi/2], \tag{4.1b}$$

No.	A_c (mm)	ω	$B^\star$ (mm)	$L^\star$ (mm)	$H^\star$ (mm)
M0	0	0	5.00	70.00	0
M1	2	$\pi/30$	4.89	70.65	0
M2	4	$\pi/30$	4.61	72.55	0
M3	6	$\pi/30$	4.24	75.55	0
M4	2	$\pi/10$	4.26	75.55	0
M5	4	$\pi/10$	3.16	89.25	0
M6	6	$\pi/10$	2.36	107.12	0
M7	2	$\pi/5$	3.29	89.25	0
M8	4	$\pi/5$	1.93	127.12	0
M9	6	$\pi/5$	1.31	170.20	0
T1	0	0	5.00	70.00	0.5
T2	0	0	5.00	70.00	1.0
T3	0	0	5.00	70.00	1.5
T4	0	0	5.00	70.00	0.5
T5	0	0	5.00	70.00	1.0
T6	0	0	5.00	70.00	1.5
H1	2	$\pi/10$	4.26	75.55	0.5
H2	2	$\pi/10$	4.26	75.55	1.0
H3	2	$\pi/10$	4.26	75.55	1.5

TABLE 2. Geometry of channel spacers.

where A_c and ω are the amplitude and period of the sinusoidal wave, respectively, and B is the membrane width. The designs T1–T6 are characterized by micropatterns composed of cylindrical posts of different heights and arrangements: T1, T2 and T3 have square (aligned) patterns with micropillars of different heights, while T4, T5 and T6 designs are characterized by staggered (hexagonal) patterns with three different pillar heights. The hybrid designs H7, H8 and H9 are a combination of morphological and topological changes with three different pattern heights. Details of all the geometries are given in figure 4 and table 2. For each geometry, we investigate the membrane response to fouling for six different inlet velocities (U_{in}) with Reynolds number,

$$Re = \frac{U_{in}B}{\nu}, \tag{4.2}$$

ranging from 250 to 1000, as listed in table 1, for a total of 114 simulations.

Example results are shown in figures 5 and 6 which provide the spatial distribution of the foulant for membrane types M0, T1, T4, M4 and H7 and two different inlet velocities. Figure 5 demonstrates how morphological or topological changes of the membrane can significantly impact foulant distribution. Additionally, a comparison between figures 5 and 6 suggests that higher inlet velocities significantly decrease foulant accumulation. This is expected since higher inlet (and local) velocities are associated with increased shear stress on the membrane, and reduced foulant accumulation. In figure 7, we plot the magnitude $|U_m|$ of the velocity at the membrane surface, averaged over the channel width, for two fixed inlet velocities and five different geometries M0, M1, M4, M7 and T1,

$$|U_m|(X) = \int_0^B \sqrt{U(X, Y, Z = H^-)^2 + V(X, Y, Z = H^-)^2}\, \mathrm{d}Y. \tag{4.3}$$

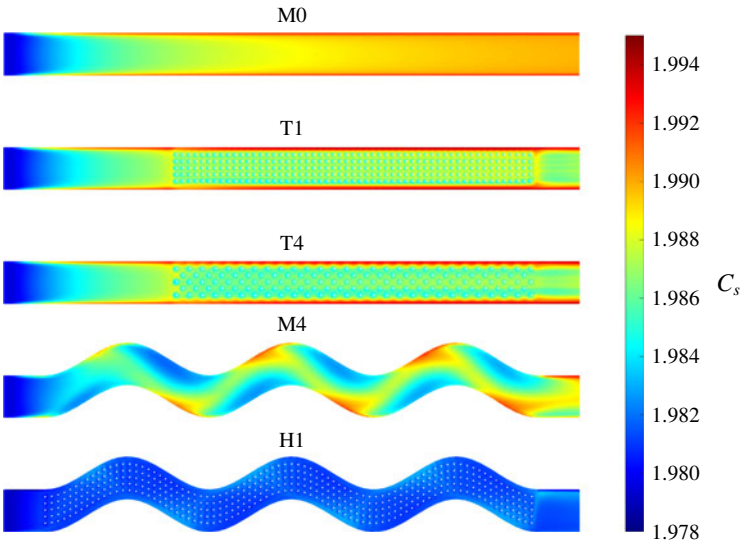

FIGURE 5. (Colour online) Steady-state foulant concentration field C_s for M0, T1, T4, M4 and H1 designs and inlet velocity $U_{in} = 0.075$ m s^{-1}.

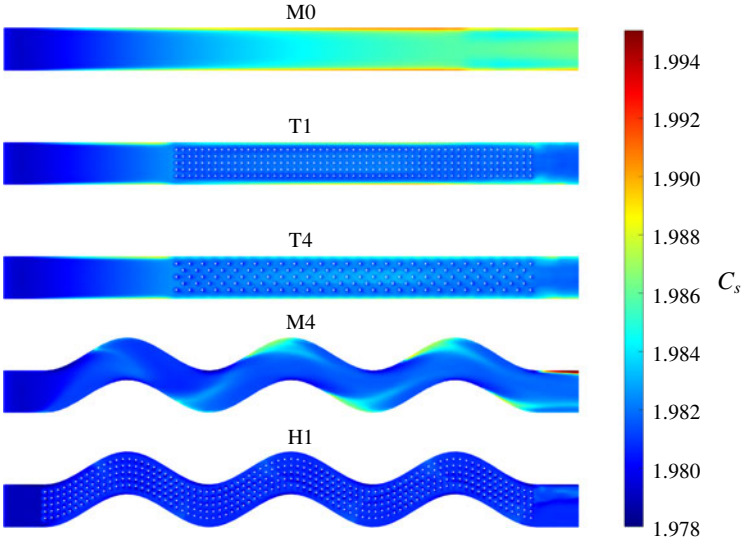

FIGURE 6. (Colour online) Steady-state foulant concentration field C_s for M0, T1, T4, M4 and H1 and inlet velocity $U_{in} = 0.2$ m s^{-1}.

Figure 7 shows that (i) the mean velocity $|U_m|(X)$ for designs M1, M4 and M7 is always higher than the straight channel design, and (ii) when the inlet velocity increases, the velocity at the membrane surface for all designs increases.

Figure 8 shows the velocity (sections 1 and 2) and concentration (section 3) distribution in three sections of channels T1 and T2, for two different inlet velocities ($U_{in} = 0.075$ m s^{-1} in (a,b), and $U_{in} = 0.2$ m s^{-1} in (c,d)). The sections are extracted as follows: sections 1 and 2 are a vertical section (parallel to the X–Z plane) and

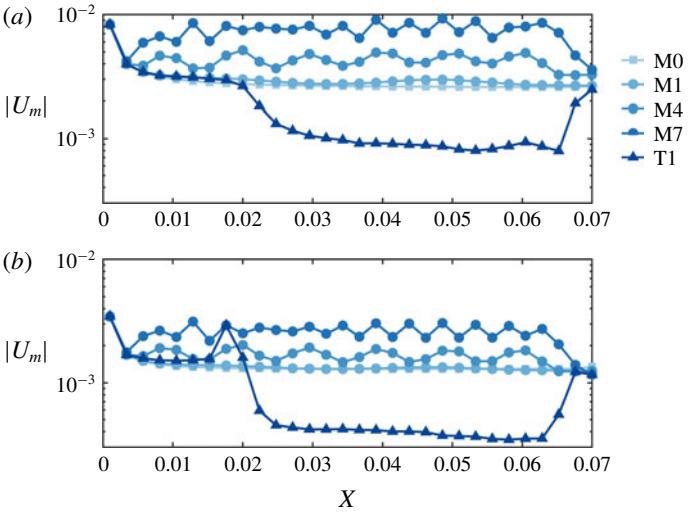

FIGURE 7. (Colour online) Velocity magnitude $|U_m|(X)$ at the membrane surface. The value is averaged along the Y-direction as defined in (4.3). (a,b) Plot $|U_m|(X)$ for two different inlet velocities $U_{in} = 0.075$ and $U_{in} = 0.15$, respectively.

a horizontal section (parallel to the X–Y plane and in proximity of the pattern's top) and show the velocity distribution; section 3, horizontal and in proximity of the membrane, shows C_b. For lower velocities (figure 8a,b), T1 and T2 both exhibit strong CP near the membrane surface with small velocity at the interface: with lower flow rates through the pattern, shear stress on the membrane decreases and foulant accumulation is promoted. Instead, for higher inlet velocities (figure 8c,d), the bulk concentration is smaller near the membrane surface for both cases. However, it is worth noticing that taller pillars, as in the T2 membrane, locally decelerate the flow and reduce antifouling efficiency, compared to their shorter counterparts (T1) where advective mixing near the membrane significantly reduces CP while providing lower flow resistance (and, consequently, pressure drop). Corresponding fouling patterns (C_s distribution) are shown in figures 5 and 6.

Additionally, unsteady simulations allow one to explore where the fouling initiates and how the foulant grows. We extract one section of the flow channel M7 for the simulation SIM-2, and plot the foulant concentration on the membrane surface C_s together with the streamlines in the channel at different instances in time, see figure 9. Figure 9 shows that when the flow field is developing, vortices form in the crests and troughs of the sinusoidal channel. At $t \approx 120$ s, foulant starts to accumulate in the channel, by first nucleating at the centre of the vortex. As time evolves, the foulant accumulation grows following a spatial pattern similar to that of the vortex. The newly developed transient solver is capable of capturing temporal variation of the synergistic effect of hydrodynamics, solute transport and surface fouling process.

4.2. *Scaling variables for rough and wiggly membranes*

The analysis of § 2.2 provides a useful, although incomplete, framework to study membrane performance: in the presence of topological or morphological alterations of the membrane, additional length scales are introduced into the problem, which

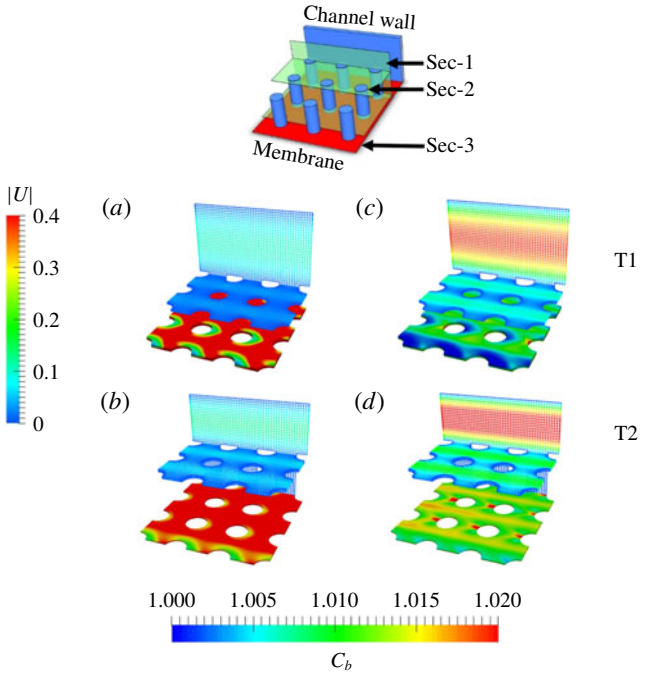

FIGURE 8. (Colour online) Velocity (sections 1 and 2) and concentration (section 3) distribution in three sections of channels T1 and T2, for two different inlet velocities ($U_{in} = 0.075$ m s^{-1} in (a,b), and $U_{in} = 0.2$ m s^{-1} in (c,d)). The sections are extracted as follows: section 1 and section 2 are a vertical section (parallel to the X–Z plane) and a horizontal section (parallel to the X–Y plane and in proximity of the pattern's top) and show the velocity distribution; section 3, horizontal and in proximity of the membrane, shows C_b.

were not taken into account in the previous analysis. Furthermore, since the input velocity and the length scales associated with the membrane alteration are the primary decision/design variables, an explicit dependence of the filtration performance index ξ on Reynolds number is desirable.

In order to quantitatively compare the impact that morphological and topological changes have on fouling, we define the following dimensionless length scales,

$$\eta = B^\star/B, \quad \text{and} \quad \zeta = (H - H^\star)/H, \tag{4.4a,b}$$

where $0 < \eta \leqslant 1$ and $0 \leqslant \xi \leqslant 1$, where $B^\star$ is the closest distance between the channel side walls and $H^\star$ is the height of the pattern in the Z-direction. For a straight channel $\eta = 1$, and for a topologically unaltered membrane $\zeta = 1$, i.e. η and ζ provide measurements of the 'waviness' of the channel and of the 'roughness' of the membrane surface, respectively. Specifically, η and ζ represent the thinnest channel neck versus the largest width that the fluid can experience in (XY)- and (YZ)-planes, respectively. Furthermore, we introduce a modified Reynolds number $Re^\star$, which accounts for topological and morphological features,

$$Re^\star = \left(\frac{1}{\eta^2 \zeta}\right) Re. \tag{4.5}$$

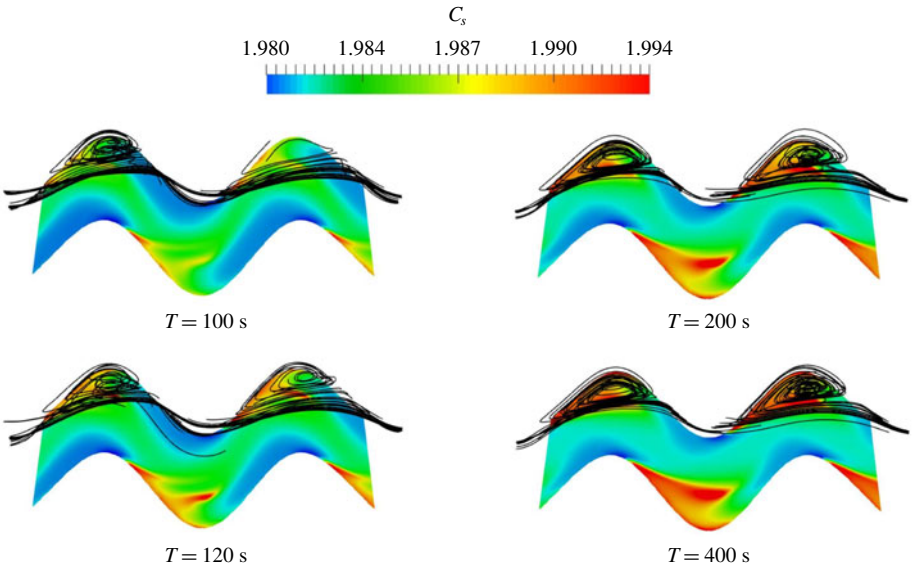

FIGURE 9. (Colour online) Foulant distribution C_s (colour field) overlaid with streamlines (solid lines) in a portion of channel M7, at four different instances in time (t = 100, 120, 200, 400 s) and for an inlet velocity $U_{in} = 0.075$ m s^{-1}.

In the following, we will show that the modified Reynolds number $Re^\star$ allows one to quantitatively compare the performance of membranes with different morphological and topological features under a unified framework. In fact, while the Be and Sh numbers represent direct estimators of membranes performance, $Re^\star$ is the primary decision variable as it concurrently prescribes inlet velocity/volumetric flux and membrane geometry.

4.3. *Scaling laws*

Since (2.44) suggests that both Be and Sh have the same scaling in terms of Reynolds number, in figure 11 we plot Sh and Be as a function of $Re^\star$ for all 114 simulations. In the insets of figure 11, we provide a plot of Sh and Be in terms of Re for comparison. Figure 11, where all the data points collapse onto one scaling curve, suggests that $Re^\star$ is an appropriate scaling variable, able to provide a unifying framework for the analysis of topologically and morphologically altered membranes.

Specifically, in figure 11(a), we plot Sh as a function of $Re^\star$, and show that appropriately rescaled data collapse reasonably well (particularly for $Re^\star > 10^3$) with Sh increasing with $Re^\star$ and an inflection point for $1000 < Re^\star < 5000$. Two scaling regimes can be identified with a transition occurring at $Re^\star \approx 1000$: in both regimes, Sh (i.e. $Q_{m,\infty}$) increases with $Re^\star$ although at different rates (with Sh increasing faster for $Re^\star < 1000$). The data suggest a parabolic scaling between Sh and $Re^\star$ for $Re^\star > 1000$, i.e.

$$Sh \sim Re^{\star 2} \quad \text{for } Re^\star > 10^3, \tag{4.6}$$

where larger inlet velocities result in larger steady-state permeate fluxes. Similarly, figure 11(b) shows the relationship between Be and $Re^\star$ with the scaling (4.6) overlaid. As hypothesized by analogy with the benchmark case, also

$$Be \sim Re^{\star 2} \quad \text{for } Re^\star > 10^3, \tag{4.7}$$

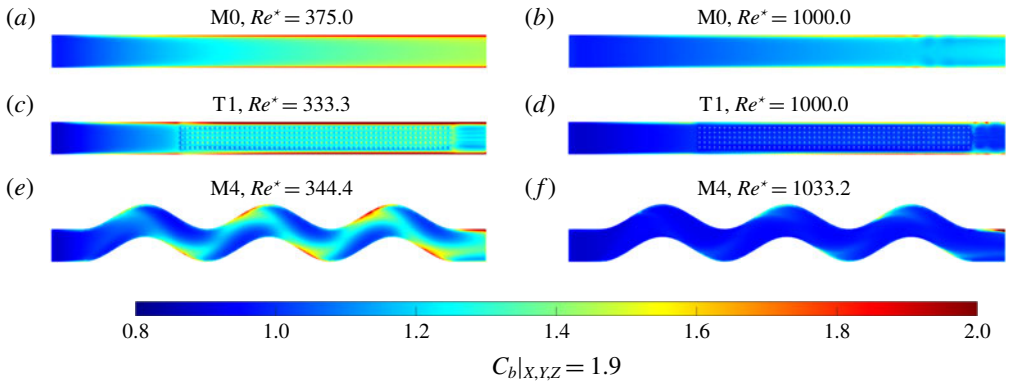

FIGURE 10. (Colour online) Bulk concentration distribution (C_b) near the membrane surface ($Z = 1.9$ mm) for two different $Re^\star$, $Re^\star \approx 300$ (a,c,e) and $Re^\star \approx 1000$ (b,d,f), and three designs, M0 (a,b), T1 (c,d) and M4 (e,f).

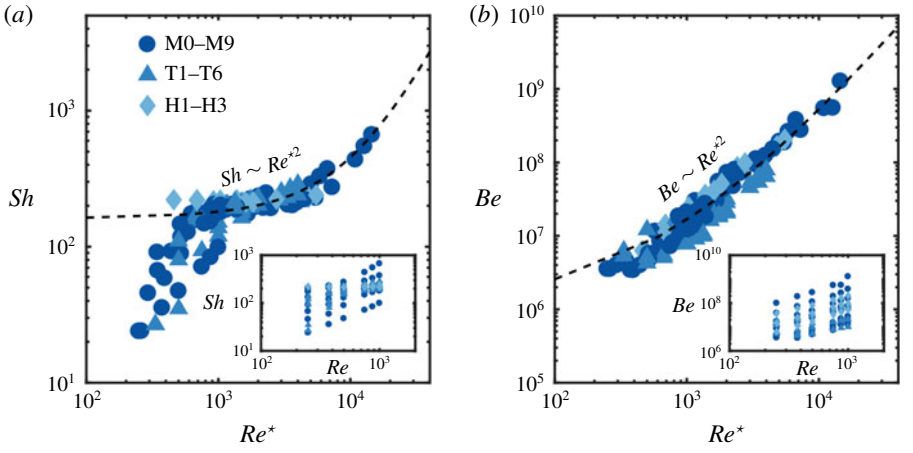

FIGURE 11. (Colour online) (a) Sherwood number (Sh) plotted as a function of the dimensionless group ($Re^\star$); (b) Bejan number (Be) plotted as a function of the dimensionless group ($Re^\star$). In both plots, the dashed line is $Be \sim Re^{\star 2}$.

i.e. larger inlet velocities result in larger overall pressure drops between the inlet and the outlet. The proposed scaling (4.7) matches the data very well.

We now proceed by numerically validating the long-time analytical scaling relationship (2.44) between Be and Sh. Bejan and Sherwood numbers are numerically determined from the pressure distribution at the inlet and the permeate flux once steady state is reached. In figure 12, we plot Sh as a function of Be for the 114 simulations (symbols).

Figure 12 confirms the scaling relationships (2.45) derived for a rectangular membrane: the analytical solution (dashed line in figure 12) matches the data points through the rescaling $\mathcal{F}(Be/800)$ for $Re^\star > 10^3$. For $Re^\star < 10^3$, as figure 10 demonstrates, the variation of the bulk concentration C_b with X and Y is not negligible, and the assumption that $C_b \approx C_b(Z)$ is not valid any longer.

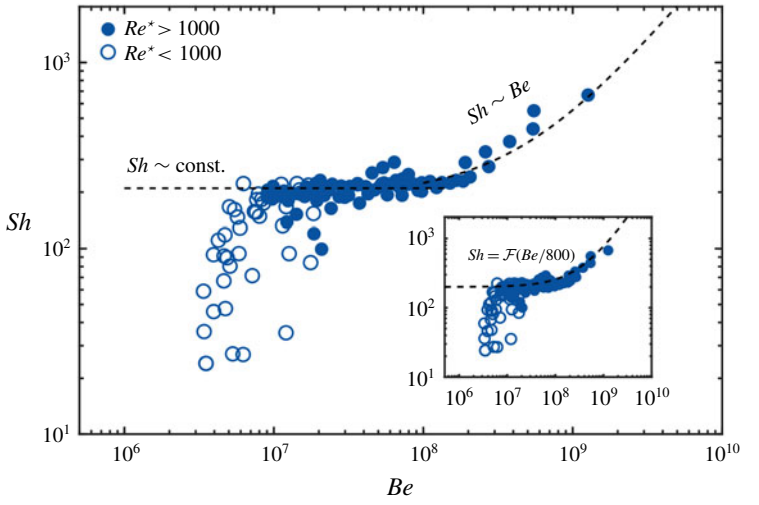

FIGURE 12. (Colour online) Sh as a function of Be for all 114 simulations (symbols). The dashed line represents the analytical scaling of (2.44). The inset shows the exact relationship needed to overlap (2.44) with the data, where the rescaling factor is $Be/800$.

4.4. *Performance index optimization*

In figure 13 we plot the membrane performance index for all 114 simulations: ξ follows a universal non-monotonic behaviour for all types of channels (types M, T and H); first, it increases with $Re^\star$ for $Re^\star < 10^3$, and then decreases for $Re^\star > 10^3$. This can be explained as follows: for $Re^\star > 10^3$, an increase in $Re^\star$ at a fixed Re corresponds to an increase of the channel waviness η, the 'roughness' height ζ or both; although these membrane alterations cause a steady increase of the permeate flux (see figure 11*a*), this effect is outweighed by the increase in pressure drop necessary to sustain the imposed volumetric rate (see figure 13). As a result, ξ decreases with a further increase in $Re^\star$, when $Re^\star > 10^3$. Instead, for $Re^\star < 10^3$, the increase in permeate flux is faster than the increase in the required pressure drop, leading to a net increase of membrane performance. Importantly, figure 13 shows that ξ has a maximum for the values of $Re^\star$ investigated, i.e. the dependence between ξ and $Re^\star$ can be used for membrane performance optimization, both in terms of design and operating conditions.

Within each membrane type (i.e. M or T), we select the design that maximizes $\xi(Re^\star)$ across the full range of $Re^\star$ investigated. Designs M4 and T1 are the best performing among the M and T designs, respectively. The overall best performing design across all categories (M, T and H) is H1, a combination of M4 and T1, although its performance is superior to all other designs for a very limited range of $Re^\star$. This demonstrates that $\xi - Re^\star$ curves can be used both to identify best performing designs within each class type (M or T) as well as to combine basic designs into hybrid ones to achieve improved performance.

Figure 14 shows ξ in terms of $Re^\star$ for M4, T1 and the reference rectangular membrane M0. Three regions can be identified based on the magnitude of $Re^\star$. In region I (i.e. at lower $Re^\star$) morphological alterations of the membrane improve the performance compared to the reference case M0; instead, topological modifications lead to underperformance compared to M0 (i.e. the 'doing nothing' option) since the

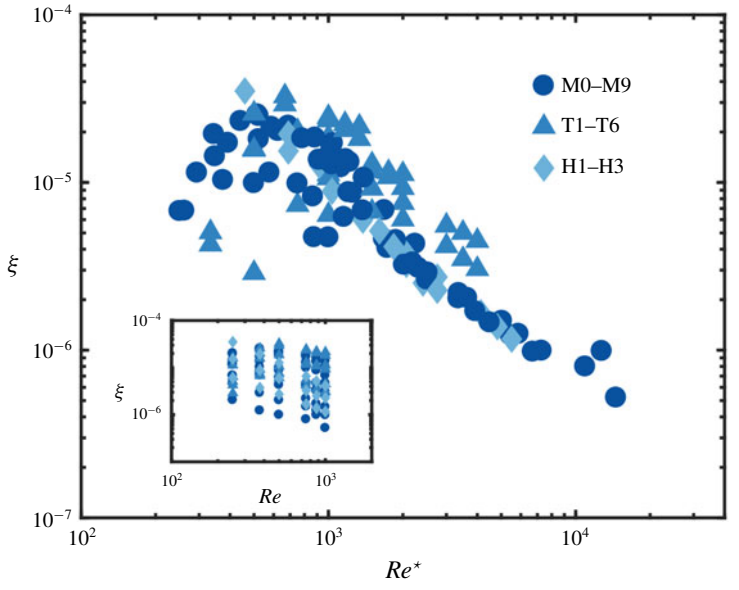

FIGURE 13. (Colour online) Performance index (ξ) plotted as a function of the dimensionless group ($Re^\star$) for all 114 simulations.

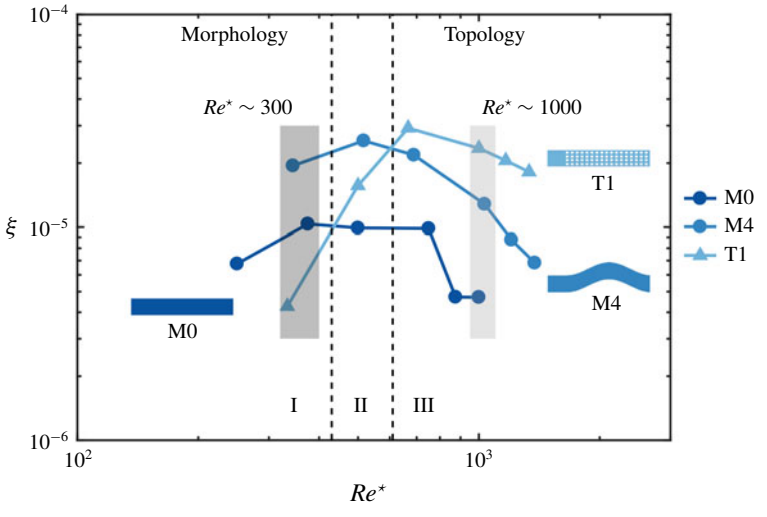

FIGURE 14. (Colour online) Membrane performance index ξ in terms of $Re^\star$ for the two best performing designs within their own class, M4 and T1, and the reference design M0. In region I, morphological modifications improve ξ compared to topological ones, which, instead, underperform compared to the 'do nothing' option M0. In region III, topological modifications outperform both the benchmark design as well as the best performing M-design.

surface pattern introduces additional roughness and promotes foulant accumulation. In region II, both M4 and T1 improve the system performance compared to M0, while M4 still outperforms T1. In region III (i.e. at higher $Re^\star$), the trend is inverted:

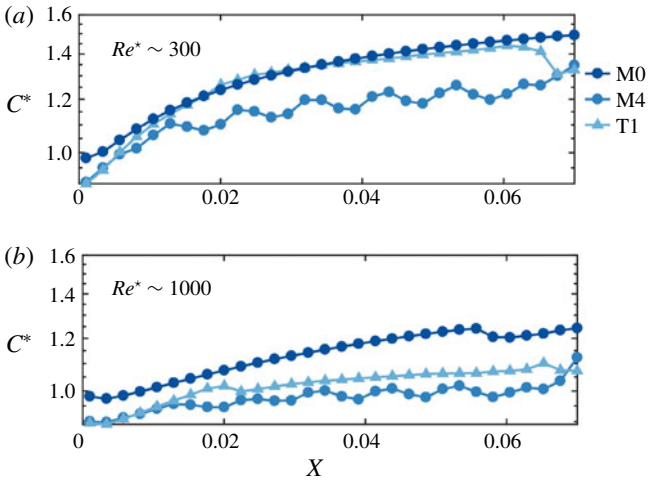

FIGURE 15. (Colour online) CP modulus $C^\star$, defined in (4.3), for M0, M4 and T1 and two values of $Re^\star$ ($Re^\star \approx 300$ top, $Re^\star \approx 1000$ bottom).

topological modifications maximize the membrane performance compared to both M0 and M4 since at higher $Re^\star$ (or velocity), surface modifications promote high permeate flux (due to an increase of local shear stress on the membrane and a concurrent decrease in foulant accumulation) while operating at a lower pressure drop compared to the morphologically altered channels. To explore the reason that causes the differences in efficiency for different patterns, in figure 15 we plot the Y-averaged concentration on the $Z = 1.9$ mm plane as a function of X, i.e. the ratio between the bulk concentration evaluated in proximity of the membrane mid-plane and the inlet concentration,

$$C^\star(X) = \int_0^B C_b(X, Y, Z = H^-)\,\mathrm{d}Y, \tag{4.8}$$

also known as the CP modulus. In figure 15, we plot $C^\star(X)$ for three different geometries (M0, M4 and T1) and two different values of $Re^\star$. When the $Re^\star < 1000$, both M0 and T1 show a high CP modulus relative to M4: as a result, M4 performs better among all the cases. Additionally, since the T1 design introduces additional shear stress near the membrane surface due to its patterned surface, it also requires a higher pressure input than that needed for the M0 case. This explains why T1's performance index is lower than that of M0. When the $Re^\star \sim 1000$, although the CP moduli of T1 and M4 are approximately the same, M4's morphology has a much larger flow resistance (i.e. higher pressure drop requirements) which results in a lower overall performance index.

5. Conclusions

Reverse osmosis membranes are employed in a variety of engineering applications, ranging from waste-water purification to desalination systems. Fouling control is crucial for both efficiency enhancement and energy saving of the filtration process. Morphological (wiggliness) and topological (roughness) modifications of the membrane have been successfully employed to reduce fouling, however optimization

of either spacer morphology, surface topology or both is still carried out by trial and error. This is due to the lack of quantitative understanding of (i) the dynamic feedbacks between solute concentration in the feed solution, foulant build up on the membrane and permeate flux and (ii) the impact of morphological and/or topological modifications on membrane fouling at prescribed operating conditions.

Here, we develop a model, and its corresponding customized 3-D solver in OpenFOAM, that couples flow, bulk and foulant surface concentration dynamically. The model and numerical solver are validated against experimental data of the permeate flux conducted by Rahardianto *et al.* (2006), who studied temporal permeate flux variation and steady-state fouling pattern formation on the membrane. The code is also able to correctly predict the experimental spatial distribution of the fouling pattern. After validation, we identify relevant dimensionless numbers involved in the problem, including the Bejan Be and the Sherwood Sh numbers which represent the dimensionless pressure drop along the channel and the dimensionless flux at steady state, the two primary variables to be optimized as they control directly membrane efficiency both in terms of energy consumption and generated clean water flux. We analytically derive the relationship between Sh and Be for a rectangular membrane and demonstrate that they exhibit the same scaling behaviour in terms of Reynolds number, i.e. Sh can be written as an explicit function of Bejan (Be), Schmidt (Sc) and Darcy (Dc) numbers, only. Two scaling behaviours are analytically identified for $Be \to 0$ and $Be \to \infty$ with the transition occurring at $Be^{\star}$. We further introduce the concept of filtration performance through the performance index ξ defined as the ratio between Sh and Be, which provides a framework to analyse the overall membrane performance both in terms of generated clean water flux and required pressure drop. The analysis derived for the benchmark rectangular membrane was then generalized to membranes with morphological and topological modifications.

Simulations conducted on 18 different designs and 6 inlet velocities included 9 designs of membranes with sinusoidal shape (M1–M9), 6 designs of membranes patterned by cylindrical posts of different heights and arrangements (T1–T6) and 3 hybrid designs combining both morphological and topological modifications (H1–H3), in addition to the benchmark case of a classical rectangular membrane (M0), for a total of 114 simulations. The simulations reveal that fouling in topological or morphological altered membranes is greatly impacted by the inlet velocity, i.e. Reynolds number, with T-type membranes better performing at high inlet velocities and M-type membranes outperforming both the benchmark M0 and T-configurations at low inlet velocities. Since the classical Reynolds number (based on the channel width length scale B) does not allow one to account for the additional length scales introduced by the membrane patterns or sinusoidal shape, in (4.5) we introduce a modified Reynolds number, $Re^{\star} = \eta^{-2}\zeta^{-1}Re$, where η $(0 < \eta \leqslant 1)$ and ζ $(0 \leqslant \zeta \leqslant 1)$ provide measurements of the 'waviness' of the channel and of the 'roughness' of the membrane surface, with $\eta = 1$ and $\zeta = 1$ for a straight channel and a topologically unaltered membrane, respectively. The modified Reynolds number allows one to quantitatively compare the performance of membranes with different morphological and topological features under a unified framework, with $Re^{\star}$ the primary decision variable as it concurrently prescribes inlet velocity/volumetric flux and membrane geometry. Numerical simulations show that $Re^{\star}$ represents an appropriate scaling variable since the calculated Be, Sh and ξ for all 114 scenarios collapse onto universal curves, especially for $Re^{\star} > 1000$, while for $Re^{\star} < 1000$ the universal scaling deteriorates particularly for $Sh = f(Re^{\star})$.

Within this framework, we test the validity of the analytical scalings for Be, Sh and ξ derived for the straight rectangular membrane benchmark (M0), and demonstrate

that ξ–$Re^\star$ curves can be successfully used to both identify best performing designs within each modification type (M or T), and also be employed to combine basic designs into hybrid ones to achieve improved performance. More importantly, our study provides applicability ranges in terms of the magnitude of $Re^\star$ within which morphological and topological modifications improve membrane efficiency (as measured by the performance index ξ). We identify three separate regions. At lower $Re^\star$, morphological changes improve the overall membrane efficiency (by reducing fouling and increasing the clean permeate flux) over the benchmark M0 and topologically altered membranes (T-designs), while the latter underperform even with respect to M0: at lower local velocities, surface roughness decreases the local velocity in proximity of the membranes and creates ideal conditions for foulant accumulation; instead, channel waviness promotes foulant segregation in the crests and troughs of the channel, while the pressure drop required to operate the system is still in check. For intermediate values of $Re^\star$, both T and M designs improve upon the benchmark, although morphological modifications still outperform (at least by a factor of 2) topological ones. For higher $Re^\star$, T designs are superior to all M designs, i.e. surface roughness significantly reduces fouling while only moderately increasing pressure drop; instead, in M-type membranes the gain in performance due to increased permeate flux is outweighed by the increase in pressure drop needed to maintain steady state.

To conclude, we proposed a new model to quantitatively analyse the impact that morphological and topological membrane modifications have both on fouling and energy input, while accounting for dynamic feedback between foulant bulk and surface concentration, permeate flux and pressure drop. To the best of our knowledge, this is the first work to propose a framework (i) that clearly relates (micro- and meso-scale) topological and morphological structure to system- (macro-) scale function/performance and (ii) within which the performance of different membrane designs can be assessed and optimized, while providing guidance on the most promising alteration types (morphological or topological) in terms of operating conditions. The ability to capture dynamic feedbacks allows one to both (i) quantify the temporal correlation between foulant deposition and local hydrodynamics (e.g. flow, stress, etc.) and (ii) employ this knowledge in the context of dynamic optimization of membrane performance. Ongoing work includes the development of 'active' methods (i.e. based on unsteady effects) as an orthogonal design axis to the more classical 'passive' tools (e.g. chemical, morphological and topological alterations of the membrane) to improve RO system performance.

Acknowledgement

I.B. gratefully acknowledges support by the National Science Foundation (NSF) through the award number 1533874, 'DMREF: An integrated multiscale modelling and experimental approach to design fouling resistant membranes'.

REFERENCES

Ba, C., Ladner, D. A. & Economy, J. 2010 Using polyelectrolyte coatings to improve fouling resistance of a positively charged nanofiltration membrane. *J. Membr. Sci.* **347** (1), 250–259.

Battiato, I. 2012 Self-similarity in coupled Brinkman/Navier–Stokes flows. *J. Fluid Mech.* **699**, 94–114.

BATTIATO, I. 2014 Effective medium theory for drag-reducing micro-patterned surfaces in turbulent ows. *Eur. Phys. J.* E **37** (3), 19–24.

BATTIATO, I., BANDARU, P. & TARTAKOVSKY, D. M. 2010 Elastic response of carbon nanotube forests to aerodynamic stresses. *Phys. Rev. Lett.* **105**, 144504.

BATTIATO, I. & RUBOL, S. 2014 Single-parameter model of vegetated aquatic flows. *Water Resour. Res.* **50** (8), 6358–6369.

BENITO, Y. & RUIZ, M. L. 2002 Reverse osmosis applied to metal finishing wastewater. *Desalination* **142** (3), 229–234.

BHATTACHARYYA, D., BACK, S. L., KERMODE, R. I. & ROCO, M. C. 1990 Prediction of concentration polarization and flux behavior in reverse osmosis by numerical analysis. *J. Membr. Sci.* **48** (2–3), 231–262.

BOWEN, W. R. & DONEVA, T. A. 2000 Atomic force microscopy studies of membranes: effect of surface roughness on double-layer interactions and particle adhesion. *J. Colloid Interface Sci.* **229** (2), 544–549.

BRIAN, P. L. T. 1965 Concentration polar zation in reverse osmosis desalination with variable flux and incomplete salt rejection. *Ind. Engng Chem. Fundam.* **4** (4), 439–445.

BRUSILOVSKY, M., BORDEN, J. & HASSON, D. 1992 Flux decline due to gypsum precipitation on ro membranes. *Desalination* **86** (2), 187–222.

BUCS, S. S., LINARES, R. V., VROUWENVELDER, J. S. & PICIOREANU, C. 2016 Biofouling in forward osmosis systems: an experimental and numerical study. *Water Res.* **106**, 86–97.

BUCS, S. S., RADU, A. I., LAVRIC, V., VROUWENVELDER, J. S. & PICIOREANU, C. 2014 Effect of different commercial feed spacers on biofouling of reverse osmosis membrane systems: a numerical study. *Desalination* **343**, 26–37.

CATH, T. Y., GORMLY, S., BEAUDRY, E. G., FLYNN, M. T., ADAMS, V. D. & CHILDRESS, A. E. 2005 Membrane contactor processes for wastewater reclamation in space: part I. Direct osmotic concentration as pretreatment for reverse osmosis. *J. Membr. Sci.* **257** (1), 85–98.

CETIN, E., EROĞLU, İ. & ÖZKAR, S. 2001 Kinetics of gypsum formation and growth during the dissolution of colemanite in sulfuric acid. *J. Cryst. Growth* **231** (4), 559–567.

CHIANESE, A., RANAURO, R. & VERDONE, N. 1999 Treatment of landfill leachate by reverse osmosis. *Water Res.* **33** (3), 647–652.

ELIMELECH, M. & PHILLIP, W. A. 2011 The future of seawater desalination: energy, technology, and the environment. *Science* **333** (6043), 712–717.

ELIMELECH, M., ZHU, X., CHILDRESS, A. E. & HONG, S. 1997 Role of membrane surface morphology in colloidal fouling of cellulose acetate and composite aromatic polyamide reverse osmosis membranes. *J. Membr. Sci.* **127** (1), 101–109.

FRITZMANN, C., LÖWENBERG, J., WINTGENS, T. & MELIN, T. 2007 State-of-the-art of reverse osmosis desalination. *Desalination* **216** (1–3), 1–76.

GREENLEE, L. F., LAWLER, D. F., FREEMAN, B. D., MARROT, B. & MOULIN, P. 2009 Reverse osmosis desalination: water sources, technology, and today's challenges. *Water Res.* **43** (9), 2317–2348.

GRIFFITH, I. M., KUMAR, A. & STEWART, P. 2014 A combined network model for membrane fouling. *J. Colloid Interface Sci.* **432**, 10–18.

GRIFFITH, I. M., KUMAR, A. & STUART, P. S. 2016 Designing asymmetric multilayered membrane filters with improved performance. *J. Membr. Sci.* **511**, 108–118.

GRIFFITHS, I. M., HOWELL, P. D. & SHIPLEY, R. J. 2013 Control and optimization of solute transport in a thin porous tube. *Phys. Fluids* **25** (3), 033101.

GUILLEN, G. & HOEK, E. M. V. 2009 Modeling the impacts of feed spacer geometry on reverse osmosis and nanofiltration processes. *Chem. Engng J.* **149** (1), 221–231.

JONES, K. L. & O'MELIA, C. R. 2000 Protein and humic acid adsorption onto hydrophilic membrane surfaces: effects of ph and ionic strength. *J. Membr. Sci.* **165** (1), 31–46.

JONSSON, G. & BOESEN, C. E. 1977 Concentration polarization in a reverse osmosis test cell. *Desalination* **21** (1), 1–10.

KANG, G., LIU, M., LIN, B., CAO, Y. & YUAN, Q. 2007*a* A novel method of surface modification on thin-film composite reverse osmosis membrane by grafting poly (ethylene glycol). *Polymer* **48** (5), 1165–1170.

KANG, G.-D., GAO, C.-J., CHEN, W.-D., JIE, X.-M., CAO, Y.-M. & YUAN, Q. 2007*b* Study on hypochlorite degradation of aromatic polyamide reverse osmosis membrane. *J. Membr. Sci.* **300** (1), 165–171.

KANG, P. K., LEE, W., LEE, S. & KIM, A. S. 2017 Origin of structural parameter inconsistency in forward osmosis models: a pore-scale cfd study. *Desalination* **421**, 47–60.

KIM, S. & HOEK, E. M. V. 2005 Modeling concentration polarization in reverse osmosis processes. *Desalination* **186** (1–3), 111–128.

LADNER, D., STEELE, M., WEIR, A., HRISTOVSKI, K. & WESTERHOFF, P. 2012 Functionalized nanoparticle interactions with polymeric membranes. *J. Hazard. Mater.* **211**, 288–295.

LEE, K. L., BAKER, R. W. & LONSDALE, H. K. 1981 Membranes for power generation by pressure-retarded osmosis. *J. Membr. Sci.* **8** (2), 141–171.

LEE, S. & LEE, C.-H. 2000 Effect of operating conditions on caso4 scale formation mechanism in nanofiltration for water softening. *Water Res.* **34** (15), 3854–3866.

LING, B., OOSTROM, M., BATTIATO, I. & TARTAKOSVKY, A. M. 2018 Hydrodynamic dispersion in thin channels with micro-structured porous walls. *Phys. Fluids* **30** (7).

LING, B., TARTAKOVSKY, A. M. & BATTIATO, I. 2016 Dispersion controlled by permeable surfaces: surface properties and scaling. *J. Fluid Mech.* **801**, 13–42.

LYSTER, E. & COHEN, Y. 2007 Numerical study of concentration polarization in a rectangular reverse osmosis membrane channel: permeate flux variation and hydrodynamic end effects. *J. Membr. Sci.* **303** (1), 140–153.

MA, S. & SONG, L. 2006 Numerical study on permeate flux enhancement by spacers in a crossflow reverse osmosis channel. *J. Membr. Sci.* **284** (1), 102–109.

MARUF, S. H., GREENBERG, A. R., PELLEGRINO, J. & DING, Y. 2014 Fabrication and characterization of a surface-patterned thin film composite membrane. *J. Membr. Sci.* **452**, 11–19.

MARUF, S. H., RICKMAN, M., WANG, L., MERSCH, J. IV, GREENBERG, A. R., PELLEGRINO, J. & DING, Y. 2013*a* Influence of sub-micron surface patterns on the deposition of model proteins during active filtration. *J. Membr. Sci.* **444**, 420–428.

MARUF, S. H., WANG, L., GREENBERG, A. R., PELLEGRINO, J. & DING, Y. 2013*b* Use of nanoimprinted surface patterns to mitigate colloidal deposition on ultrafiltration membranes. *J. Membr. Sci.* **428**, 598–607.

MATIN, A., KHAN, Z., ZAIDI, S. M. J. & BOYCE, M. C. 2011 Biofouling in reverse osmosis membranes for seawater desalination: phenomena and prevention. *Desalination* **281**, 1–16.

MCCOOL, B. C., RAHARDIANTO, A., FARIA, J., KOVAC, K., LARA, D. & COHEN, Y. 2010 Feasibility of reverse osmosis desalination of brackish agricultural drainage water in the san joaquin valley. *Desalination* **261** (3), 240–250.

MCCUTCHEON, J. R. & ELIMELECH, M. 2006 Influence of concentrative and dilutive internal concentration polarization on flux behavior in forward osmosis. *J. Membr. Sci.* **284** (1), 237–247.

PARK, H. B., KAMCEV, J., ROBESON, L. M., ELIMELECH, M. & FREEMAN, B. D. 2017 Maximizing the right stuff: the trade-off between membrane permeability and selectivity. *Science* **356** (6343), eaab0530.

PARK, M. & KIM, J. H. 2013 Numerical analysis of spacer impacts on forward osmosis membrane process using concentration polarization index. *J. Membr. Sci.* **427**, 10–20.

PETERS, T. A. 1998 Purification of landfill leachate with reverse osmosis and nanofiltration. *Desalination* **119** (1–3), 289–293.

RAHARDIANTO, A., MCCOOL, B. C. & COHEN, Y. 2008 Reverse osmosis desalting of inland brackish water of high gypsum scaling propensity: kinetics and mitigation of membrane mineral scaling. *Environ. Sci. Technol.* **42** (12), 4292–4297.

RAHARDIANTO, A., MCCOOL, B. C. & COHEN, Y. 2010 Accelerated desupersaturation of reverse osmosis concentrate by chemically-enhanced seeded precipitation. *Desalination* **264** (3), 256–267.

RAHARDIANTO, A., SHIH, W.-Y., LEE, R.-W. & COHEN, Y. 2006 Diagnostic characterization of gypsum scale formation and control in RO membrane desalination of brackish water. *J. Membr. Sci.* **279** (1), 655–668.

RUBOL, S., BATTIATO, I. & DE BARROS, F. P. J. 2016 Vertical dispersion in vegetated shear flows. *Water Resour. Res.* **52** (10), 8066–8080.

RUBOL, S., LING, B. & BATTIATO, I. 2018 Universal scaling-law for flow resistance over canopies with complex morphology. *Sci. Rep.* **8** (1), 4430–4445.

SABLANI, S. S., GOOSEN, M. F., AL-BELUSHI, R. & WILF, M. 2001 Concentration polarization in ultrafiltration and reverse osmosis: a critical review. *Desalination* **141** (3), 269–289.

SAGIV, A., ZHU, A., CHRISTOFIDES, P. D., COHEN, Y. & SEMIAT, R. 2014 Analysis of forward osmosis desalination via two-dimensional fem model. *J. Membr. Sci.* **464**, 161–172.

SANAEI, P. & CUMMINGS, L. J. 2017 Flow and fouling in membrane filters: effects of membrane morphology. *J. Fluid Mech.* **818**, 744–771.

SANAEI, P., RICHARDSON, G. W., WITELSKI, T. & CUMMINGS, L. J. 2016 Flow and fouling in a pleated membrane filter. *J. Fluid Mech.* **795**, 36–59.

SANEI, P. & CUMMINGS, L. J. 2018 Membrane filtration with complex branching pore morphology. *Phys. Rev. Fluid* **3** (094305).

SHANNON, M. A., BOHN, P. W., ELIMELECH, M., GEORGIADIS, J. G., MARIÑAS, B. J. & MAYES, A. M. 2008 Science and technology for water purification in the coming decades. *Nature* **452** (7185), 301–310.

SHEIKHOLESLAMI, R. & ONG, H. W. K. 2003 Kinetics and thermodynamics of calcium carbonate and calcium sulfate at salinities up to 1.5 m. *Desalination* **157** (1–3), 217–234.

SHIH, W.-Y., RAHARDIANTO, A., LEE, R.-W. & COHEN, Y. 2005 Morphometric characterization of calcium sulfate dihydrate (gypsum) scale on reverse osmosis membranes. *J. Membr. Sci.* **252** (1), 253–263.

SUWARNO, S. R., CHEN, X., CHONG, T. H., PUSPITASARI, V. L., MCDOUGALD, D., COHEN, Y., RICE, S. A. & FANE, A. G. 2012 The impact of flux and spacers on biofilm development on reverse osmosis membranes. *J. Membr. Sci.* **405**, 219–232.

TAKATORI, S. C. & BRADY, J. F. 2017 Inertial effects on the stress generation of active fluids. *Phys. Rev. Fluid.* **2** (9), 094305.

VRIJENHOEK, E. M., HONG, S. & ELIMELECH, M. 2001 Influence of membrane surface properties on initial rate of colloidal fouling of reverse osmosis and nanofiltration membranes. *J. Membr. Sci.* **188** (1), 115–128.

XIE, P., MURDOCH, L. C. & LADNER, D. A. 2014 Hydrodynamics of sinusoidal spacers for improved reverse osmosis performance. *J. Membr. Sci.* **453**, 92–99.

ZHANG, R., LIU, Y., HE, M., SU, Y., ZHAO, X., ELIMELECH, M. & JIANG, Z. 2016 Antifouling membranes for sustainable water purification: strategies and mechanisms. *Chem. Soc. Rev.* **45**, 5888–5924.